Engine dynamics - challenges and opportunities for naval DC distribution grids and variable speed generators

D. van der Woude, BSc [a*], Ir. J. Vollbrandt[a,b], Dr. Ir. R.D. Geertsma, CEng, FIMarEST[a,b], Dr. A. Coraddu, MSc, CEng, MIMarEST[b], Prof. Dr. Ir. R.G. van de Ketterij[a]
[a]*Netherlands Defence Academy, The Netherlands;* [b]*Delft University of Technology, The Netherlands*
[*]Corresponding author. Email: D.vd.Woude.05@mindef.nl
Word count: 4924

Synopsis

The next generation Anti-Submarine Warfare Frigates (ASWF) of the Royal Dutch Navy is currently under development. With these new vessels, the navy aims to enhance its capability to continue structural long-term deployments. Besides facilitating directed-energy weapons and a high powered sensor suite, the vessels will also embrace a sophisticated signature management system. These technologies require a highly efficient and smart electric power generation and distribution system and the new vessels will therefore be equipped with DC distribution grids and variable speed generator sets. While variable speed generator sets offer increased efficiency and control possibilities compared to fixed speed generators, they may suffer from the lower dynamic performance of the internal combustion engine driving the generator at variable speed. Depending on the engine's operating point within the operating envelope, a sudden load change might not only demand an increased torque from the engine but also an increased rotational speed. Increasing the engine speed simultaneously requests additional torque and can push the engine beyond its operational envelope, causing increased emissions of particulate matter, high thermal engine loading or even compressor surging in the turbocharger. Since DC distribution grids do not require a fixed grid frequency, larger transient tolerances of engine speed are allowed. Especially in combination with Energy Storage Systems (ESS), DC distribution grids might be able to handle larger sudden load increases compared to classical AC distribution grids. In this paper, we address the implications of DC distribution grids and variable speed generation on the internal combustion engine with an emphasis on the dynamic response characteristic of the engine. The study investigates different strategies for load sharing in combination with an ESS to improve the dynamic response characteristic. We will discuss the effects of these load sharing strategies on the air-excess ratio and thermal loading, aiming for a reduction in the emission of particulate matter and soot, and a reduction in engine degradation. For this study, experiments on a variable speed generating set were conducted and combined with simulation experiments with an extended Mean Value First Principle (MVFP) engine model. Our results indicate that the dynamic response characteristics of the engine can be improved by carefully considering the load sharing strategies of the ship's electric power distribution system. Moreover, emissions of particulate matter and soot, as well as exhaust gas temperatures, can be reduced, decreasing the signatures of the vessels.

Keywords: Transient performance; DC distribution grids; Variable Speed Generation; Modeling and simulation; Mean value first principle model;

1 Introduction

Modern naval operations are evolving in response to intensifying geopolitical tensions and the emergence of multi-domain threats such as hypersonic missiles, loitering munitions, and a variety of aerial, surface, and subsurface drones. These threats increase the risk and complexity of maintaining secure supply lines, making logistical support and fuel resupply more vulnerable to disruption. In this context, European and North American navies are prioritizing sustained, long-term deployments with minimal logistical dependence (Voth et al., 2024). Reducing reliance on fossil fuels also aligns with a broader strategic objective: decreasing dependency on geopolitically

Authors' Biographies
Sub Lt David van der Woude currently is a student of the Royal Netherlands Naval College. In September 2025 he will start a master Marine Technology at Delft University of Technology.
Jasper Vollbrandt currently is PhD researcher at Delft University of Technology and Netherlands Defence Academy on dynamic behaviour of alternately fueled internal combustion engines. He has previously worked on ship propulsion systems for the Materiel and IT Command (COMMIT) of the Dutch Ministry of Defence and as a project engineer hydraulics for TATA Steel Netherlands.
Capt (E) Rinze Geertsma currently is associate professor at the Netherlands Defence Academy and research fellow at Delft University of Technology with a research interest in military energy systems. He previously has been Marine Engineering Officer of HNLMS de Ruyter and HNLMS Tromp. Earlier experience include system and project engineering and innovation roles.
Prof. Andrea Coraddu is an Associate Professor in the Department of Maritime and Transport Technology at Delft University of Technology. In 2012, he was awarded a Laurea and a PhD in Naval Architecture and Marine Engineering at the University of Genoa. His research lies at the forefront of the maritime energy transition, delving into the topology design, performance optimization, and control of hybrid and full electric marine energy systems.
Prof. Robert van de Ketterij is currently the chair of the section Military Technology and Sciences at the Netherlands Defence Academy and responsible for research and development in the field of systems engineering. Earlier experience includes managing director of Royal IHC - MTI Holland B.V., responsible for the Knowledge Centre regarding dredging, mining and deep-sea mining processes.

unstable and often unreliable oil-exporting countries. Reflecting this shift, the Dutch Ministry of Defence, in its 2024 Defence White Paper, announced its intention to invest in new Anti-Submarine Warfare Frigates (ASWF) designed for energy-efficient, low-signature operations over extended periods (Brekelmans, 2024).

Energy has become a critical operational resource, particularly with the anticipated integration of energy-intensive technologies such as direct energy weapons, advanced sensors, and deployable unmanned platforms (Smith, 2019; Stutevant et al., 2022). To meet these challenges, the Royal Netherlands Navy has adopted a hybrid propulsion architecture combined with a Direct Current (DC) power network (Schulten et al., 2017; Drakoulas et al., 2022; Van't Hart et al., 2024). This approach not only improves fuel efficiency and operational flexibility but also supports thermal and acoustic signature reduction—a key requirement in modern anti-submarine warfare, vital for stealth operations (Zak, 2008; Voskuijl et al., 2020).

A key enabler of this transition is the implementation of Variable Speed Generators (VSGs). Unlike traditional fixed-speed Alternating Current (AC) generators, VSGs can vary engine speed with load demand, allowing operation near optimal efficiency points (Zahedi et al., 2014). This leads to average fuel savings of around 8% and offers the additional tactical benefit of altering acoustic signatures by changing engine speeds (Zak, 2008). When integrated with onboard Energy Storage Systems (ESS), these DC-based architectures also provide a robust solution to managing the large and rapid load variations expected from future systems such as railguns and high-powered lasers (Whitelegg et al., 2014; Gattozzi et al., 2015; Farrier and Bucknall, 2020).

However, these advantages introduce new challenges. VSGs exhibit slower transient response under dynamic load conditions due to factors like turbo lag and engine inertia (Roos, 2025). This can result in suboptimal air–fuel ratios, incomplete combustion, increased thermal loading, higher emissions, and elevated acoustic and infrared signatures. Although current research significantly progressed development of energy management strategies, such as Model Predictive Control and online optimization (Bø et al., 2019; Haseltalab et al., 2019), these often overlook the dynamic behavior of individual subsystems like VSGs. Understanding and addressing these transient limitations is essential to fully unlocking the potential of hybrid naval power systems.

Previous research has demonstrated that hybrid propulsion architectures can significantly enhance fuel efficiency and operational flexibility in naval vessels. Schulten et al. (2017), building on the control framework proposed by Geertsma et al. (2017a), showed that hybrid systems employing diesel engines for high-speed propulsion—rather than conventional gas turbines—can reduce fuel consumption in frigates by up to 29%. Their concept leverages advanced control modes, such as power take-off (PTO) and power take-in (PTI), to optimise engine utilisation and reduce total operating hours. However, this work is confined to an AC-based power architecture, which imposes fixed-speed operation and inherently limits further efficiency gains.

Zahedi et al. (2014) investigated a hybrid DC power system in the context of an offshore support vessel, reporting fuel savings of up to 15% compared to its AC counterpart. These findings have been experimentally validated by Kim and Jeon (2022) using an AC/DC generator testbed, who attributed the increased efficiency to the ability of DC systems to allow generators to operate closer to their optimal fuel-efficiency points, while ESS provide short-term reserve capacity, particularly during generator outages. These outcomes suggest that comparable efficiency gains may be realised in naval frigates through the adoption of hybrid DC propulsion architectures.

A significant gap persists in the literature: most existing studies focus on steady-state performance and average fuel savings, with limited consideration given to the dynamic behaviour of diesel generators within DC-based systems. Mobarra et al. (2022) proposed the integration of ESS—such as batteries or supercapacitors—as a mitigation strategy, but did not provide a detailed analysis of the generator's dynamic load response.

Boujelben and Trigui (2021) and Bellache et al. (2017) examined dynamic control of variable speed generation in hybrid electric vehicles using ESS. These studies omitted the dynamic limitations of the internal combustion engine, or introduced delay approximations for fuel actuation and combustion, thereby overlooking important engine-specific transient phenomena caused by the turbocharger.

Iwanski et al. (2018) investigated control strategies for VSGs using a sophisticated generator model; but the engine model employed was unable to capture critical diesel engine dynamics, because the underlying mechanisms—such as air-fuel ratio imbalance or turbocharger lag—were not explored.

Ayers (2022) highlighted fast electrical dynamics, including DC bus short circuits, but neglected the internal combustion engine's dynamic limitations altogether. Similarly, Saponaro et al. (2022) developed a simulation framework including engine and generator models with dedicated controllers, but dynamic behaviour was restricted to the fuel controller and constrained by steady-state torque limits. The model was unable to represent thermal loading effects or transient trends in charge pressure.

A promising study by Roos (2025); Roos et al. (2025) incorporated a mean-value engine model derived from Geertsma et al. (2017b) to study the dynamic performance of VSGs. They concluded that the diesel engine—rather than the generator or power electronics—is the primary limiting factor in handling large load transients. In particular, the turbocharger was identified as a key bottleneck but the turbocharger model used was too simplistic to capture the full range of transient behaviour under varied operating conditions, as further discussed in (Vollbrandt

et al., 2025).

This study investigates the dynamic performance of VSG architectures, focussing on the internal combustion engine as a key limiting component. We identified critical performance bottlenecks and explored mitigation strategies to enhance the resilience, efficiency, and stealth characteristics of naval power systems. To this end, we adapted and extended an existing, validated physics-based simulation framework. The enhanced model was re-validated and employed to simulate the dynamic response of a VSG system under rapid and high-magnitude load variations. This study contributes several novel insights:

- We present and validate a modelling methodology capable of predicting the dynamic behaviour of a large, high-speed, spark-ignited marine gas engine operating under variable speed and load conditions.
- We demonstrate the necessity of incorporating ESS in VSG-based DC power architectures to prevent engine overloading during transient load events.
- We propose control principles for coordinated ESS and VSG operation that significantly improve load response, reduce thermal stress, and mitigate signature-related emissions, relative to conventional fixed-speed AC generator sets.

2 Theoretical Framework

2.1 SI engines for marine applications

The engine investigated in this study is a Caterpillar 3508A high-speed, four-stroke, spark-ignited (SI) gas engine, operated by the engine laboratory of the Netherlands Defense Academy (NLDA) in Den Helder. Publications (Vollbrandt et al., 2024; Kiouranakis et al., 2025) describe the data acquisition of this engine. It currently runs on natural gas from the grid, and has previously been operated on methanol and various blends of natural gas and hydrogen (Sapra et al., 2019; Bosklopper et al., 2020). This engine serves as a representative example of a marine SI engine capable of operating on 100 % alternative fuels.

To avoid knocking or misfiring, SI engines require a tightly controlled air-excess ratio λ. In contrast, marine compression-ignited (CI) engines are less susceptible to such phenomena and can operate across a broader range of air-excess ratios. Nevertheless, maintaining a stable λ in CI engines helps reduce excessive thermal loading and emissions, thereby minimising engine wear and thermal signatures. As a result, naval CI engines may benefit from control strategies originally developed for SI engines, suggesting that findings from this study could be transferable. A detailed comparison between SI and CI engine control, however, lies beyond the scope of this work.

2.2 The Mean Value First Principle Engine Model

The implemented MVFPEM is based on the comprehensive framework described by Vollbrandt et al. (2025), with a block diagram shown in Figure 1. The gas path is modelled using the filling-and-emptying approach (Horlock and Winterbone, 1986), represented by three control volumes. A complete turbocharger model is incorporated, with performance parameters determined using the methodology developed by Stapersma (2019). The in-cylinder combustion process is not resolved on a crank-angle basis; instead, averaged in-cylinder parameters are estimated using a six-point Seiliger cycle model (Seiliger, 1926).

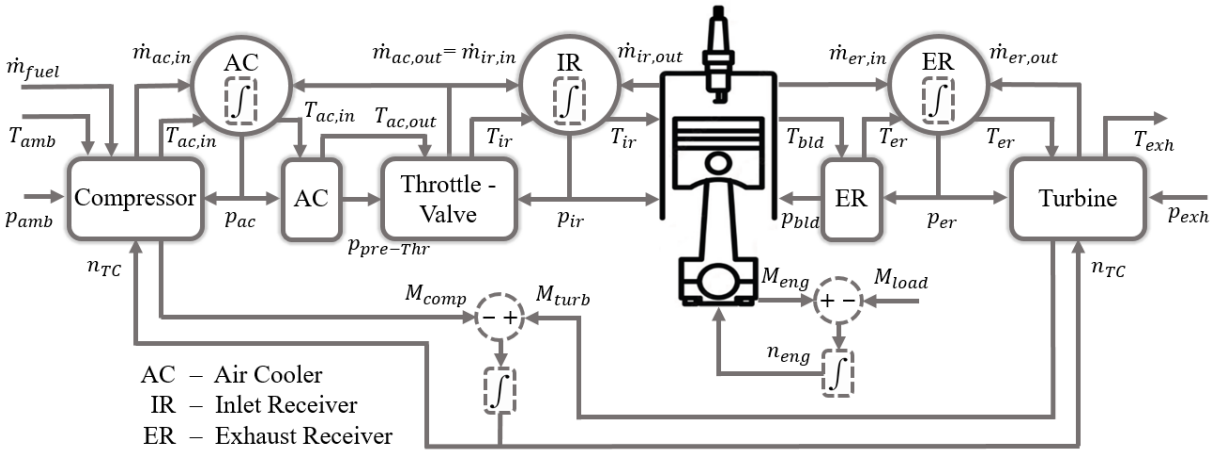

Figure 1: Block diagram of the implemented MVFPEM (Vollbrandt et al., 2025).

To enable the analysis of a variable-speed generator set, we extended the model to operate across a range of engine speeds and to accurately capture dynamic responses to variations in engine load and speed. This includes

modifications to the in-cylinder process (Subsection 2.4) and the calibration of the turbocharger model (Subsection 2.5.) The adapted model is calibrated using 25 steady-state operating points, covering five engine speeds and five load levels. Figure 2 illustrates this 5×5 measurement grid. Following Roos (2025), generator efficiency is assumed to remain relatively constant over different load and speed conditions; hence, the generator is not explicitly modelled, but its efficiency is included in the engine's overall mechanical efficiency.

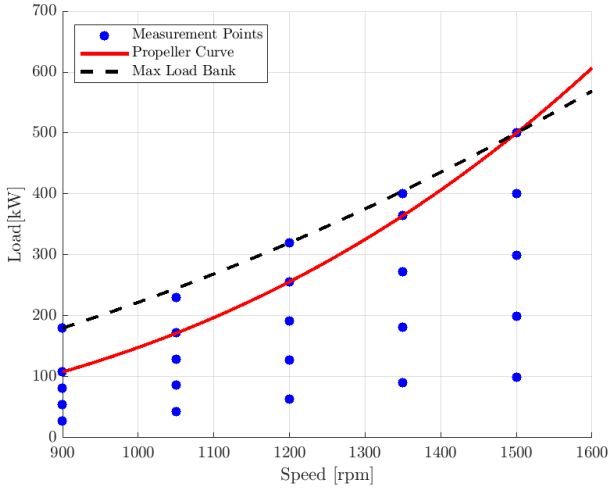

Figure 2: Grid of measurement points shown within the engine envelope together with the maximum load of the load bank and the propeller curve.

2.3 Engine and VSG control principles

Engine control consists of two main components: the throttle valve and the TecJet gas valve. The throttle valve regulates engine speed by restricting the mass flow of the air-fuel mixture from the compressor to the inlet receiver. The TecJet valve adjusts fuel flow upstream of the compressor, based on predefined fuel mapping values (air-excess ratio) provided in Table 6. Engine speed is the only user-defined input; all other parameters are automatically controlled via preset mappings and closed-loop regulation. A more comprehensive description of the engine control is given in (Vollbrandt et al., 2025).

The VSG was studied as part of a hybrid DC power system, configured as shown in Figure 3. In this setup, the system was subjected to predefined load steps, though in real-world applications, power demand is dynamic. The generator output is regulated via an AC-DC converter to meet a specified power setpoint. The battery ESS dynamically compensates for any difference between the load and generator output. This introduces a second control variable — generator load — in addition to engine speed.

During variable-speed operation, the engine speed setpoint is selected to minimise fuel consumption. Figure 4, which shows brake-specific fuel consumption (BSFC) across all calibrated operating points within the engine's operational envelope, illustrates this. The blue curve indicates the optimal engine speed for each load point. At low speeds, this curve deviates from the absolute optimum to maintain a safety margin 0f 10% from engine operating limits.

2.4 Modelling in-cylinder process

A MVFPEM calculates the average exhaust gas parameters based on the inlet gas and the required power output of the engine. The average thermodynamic parameters are determined using a six-point Seiliger cycle (Seiliger, 1926), with heat release functions implemented according to Geertsma et al. (2017b).

The Seiliger cycle does not account for the exhaust and intake strokes, which contribute to scavenging losses. These losses are usually negligible, but become significant at low loads. For a load of 100 kW at 1500 rpm, the scavenging losses are about 11% of the total work done within the cycle. To take these losses into account, these strokes are modelled as constant pressure, during the exhaust stroke at the exhaust pressure p_{exh} and during the inlet at the manifold air pressure (MAP) p_{in}. The total work done by the intake and exhaust strokes is calculated as:

$$w_{scavenging} = (p_{exh} - p_{in}) \cdot (V_1 - V_2) \tag{1}$$

where V_1 is the volume at Bottom Dead Centre and V_2 is the volume at Top Dead Centre. Figure 5 depicts the size of the pumping losses compared to the total indicated work done within the cylinder.

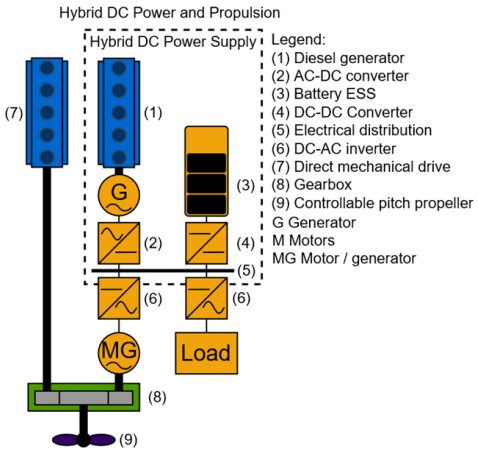

Figure 3: Hybrid propulsion architecture, adapted from (Roos, 2025).

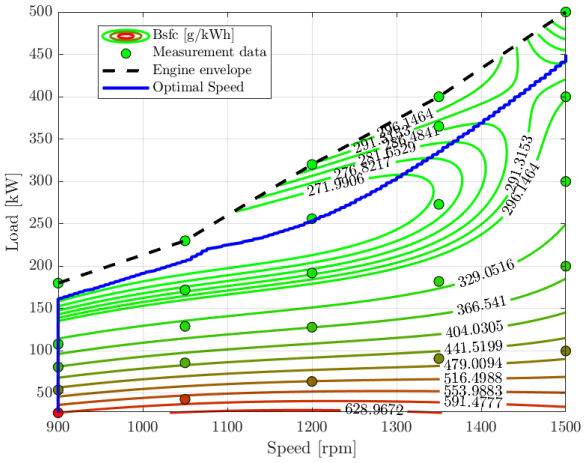

Figure 4: Brake Specific Fuel Consumption plot with optimum speed line.

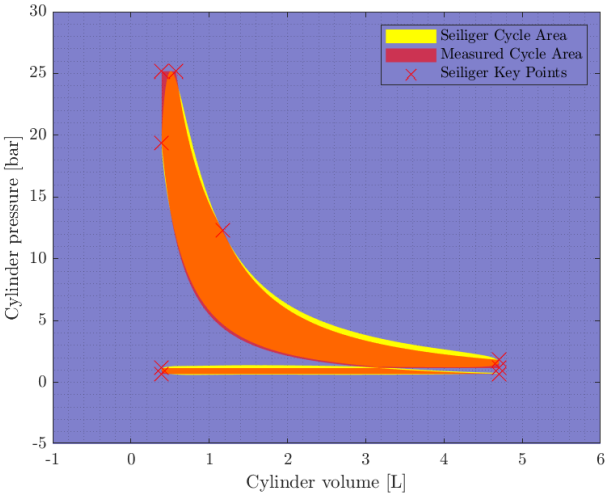

Figure 5: Indicator diagram at 900 rpm and 27 kW.

Calibration of the in-cylinder process involved tuning both the mechanical efficiency η_m and the fraction of heat released at constant pressure X_{cp} at each operating point. Mechanical efficiency was adjusted to align the calculated engine power with the measured output, while X_{cp} was tuned to match the simulated exhaust temperature with experimental data. Using these calibrated values and the in-cylinder pressure measurements, the Seiliger cycle parameters a, b, and the combustion efficiency η_q were derived. A third-degree polynomial surface fit was applied to η_m, a, b, and η_q as functions of fuel consumption and engine speed. These fitted surfaces, shown in Figure 6, serve as inputs for the in-cylinder process in the engine model.

2.5 Turbocharger Calibration

Calibration of the compressor and turbine performance models, based on the approach of Stapersma (2019), was cast as a bounded nonlinear least-squares estimation problem. The objective was to identify the parameter vector $\theta \in \mathbb{R}^8$ that minimises the discrepancy between model-predicted and experimentally observed pressure ratios over a dataset comprising $N = 25$ measurement points (see Section 2.2). The parameter vector θ is defined as:

$$\theta = \begin{bmatrix} n_0 & \dot{m}_0 & \pi_0 & \psi_0 & Ma_0 & x & y & T_{in,0} \end{bmatrix}^\top \in \mathbb{R}^8, \tag{2}$$

where n_0 is the nominal shaft speed, $\dot{m}_0$ the reference mass flow, π_0 the nominal pressure ratio, ψ_0 the enthalpy coefficient, Ma_0 the Mach number at reference conditions, x and y are shape sensitivity parameters, and $T_{in,0}$ the nominal inlet temperature.

The calibration task is formulated as a bounded nonlinear least-squares problem:

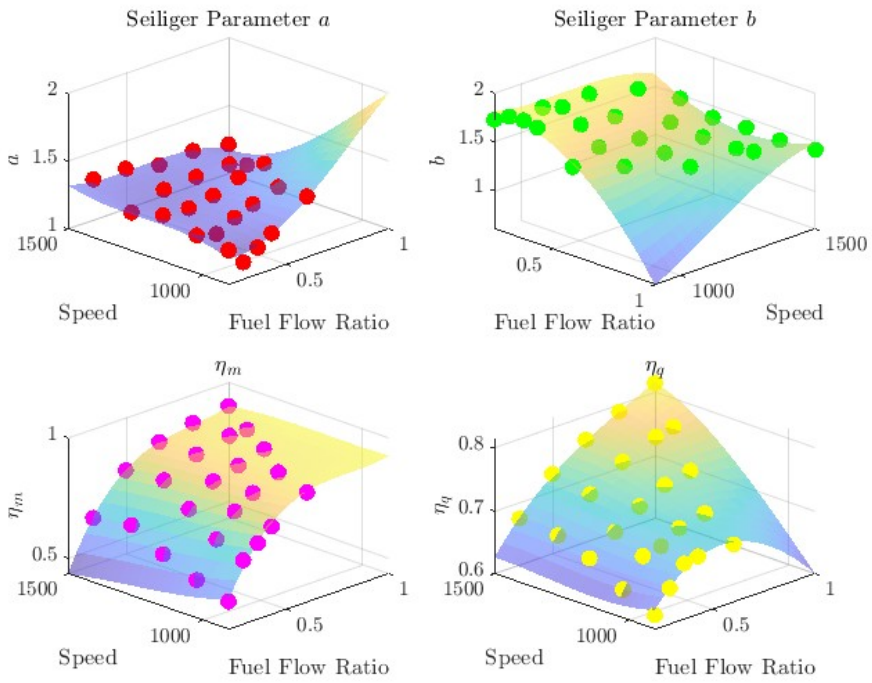

Figure 6: Polynomial fit of parameters.

$$\min_{\theta \in \mathscr{B}} \; J(\theta) := \left\| \mathbf{W}^{1/2} \left(\pi^{\text{model}}(\theta) - \pi^{\text{meas}} \right) \right\|_2^2, \tag{3}$$

where $\pi^{\text{model}}(\theta) \in \mathbb{R}^N$ is the vector of model-predicted pressure ratios evaluated at $N = 25$ measurement points, and $\pi^{\text{meas}} \in \mathbb{R}^N$ is the corresponding vector of experimental observations. The weight matrix $\mathbf{W} = \text{diag}(w_1, \ldots, w_N)$ encodes the relative confidence in each data point; in this work, uniform weights $w_i = 1$ are applied.

The admissible parameter set $\mathscr{B} \subset \mathbb{R}^8$ is a box constraint defined as:

$$\mathscr{B} := \left\{ \theta \in \mathbb{R}^8 \;\middle|\; \theta^{\text{lower}} \leq \theta \leq \theta^{\text{upper}} \right\}, \tag{4}$$

where inequalities are interpreted componentwise.

To ensure physical plausibility and numerical stability of the estimation procedure, each parameter in the vector θ is constrained within predefined lower and upper bounds, forming a box-constrained admissible set $\mathscr{B} \subset \mathbb{R}^8$ (see Eq. (4)). These bounds reflect prior knowledge derived from engineering judgment, empirical correlations, and expected operating conditions of the compressor and turbine components. The complete specification of the parameter intervals is reported in Table 1, including physical units and descriptions for clarity.

Table 1: Lower and upper bounds for the parameter vector θ

Parameter	θ^{lower}	θ^{upper}
Nominal shaft speed n_0 [rpm]	65000	72000
Reference mass flow $\dot{m}_0$ [kg/s]	0.2	0.4
Nominal pressure ratio π_0 [-]	1.5	1.8
Enthalpy coefficient ψ_0 [-]	0.4	0.8
Nominal Mach number Ma_0 [-]	0.1	0.8
Sensitivity parameter x [-]	2.0	4.0
Sensitivity parameter y [-]	0.1	1.1
Inlet temperature $T_{in,0}$ [°C]	20	40

To solve the nonlinear parameter estimation problem defined in Eq. (3), a two-stage optimisation strategy was employed to balance global exploration with local convergence accuracy. The underlying objective function is non-convex, potentially non-smooth, and incorporates empirical correlations, interpolated maps, and thermodynamic

constraints. These features preclude reliance on gradient-based solvers without appropriate safeguards against local minima and poor conditioning.

As a first stage, a global search was performed using a population-based metaheuristic inspired by swarm intelligence, namely Particle Swarm Optimisation (PSO) (Kennedy and Eberhart, 1995). PSO maintains a set of candidate solutions (particles) that explore the search space $\mathscr{B}$ in parallel, updating their trajectories based on a combination of individual and collective experience. Its derivative-free nature and inherent robustness make it well-suited for high-dimensional, nonconvex, and black-box problems frequently encountered in engineering calibration (Kalikatzarakis et al., 2021). The algorithm has been shown to offer competitive performance for model identification tasks involving noisy objectives and loosely structured feasible regions (Eberhart and Shi, 2001).

Upon completion of the global phase, the best candidate parameter vector was passed to a second-stage local optimisation procedure based on Sequential Quadratic Programming (SQP) (Nocedal and Wright, 2006). SQP methods solve a series of quadratic subproblems that locally approximate the nonlinear objective and enforce box constraints via Lagrange multipliers and active-set strategies. Under mild regularity assumptions, SQP algorithms exhibit superlinear convergence near the solution, provided the initialisation is sufficiently close to a local optimum.

This hybrid strategy, combining a global stochastic search with a local gradient-based refinement, leverages the complementary strengths of both approaches: the ability to escape poor-quality basins of attraction and the efficiency of second-order local descent methods for fine-tuning. Such strategies have been widely adopted in the calibration of nonlinear models in marine applications (Kalikatzarakis et al., 2021).

The resulting optimised parameter vectors for the compressor and turbine models are reported in Table 2.

Table 2: Optimised parameter vectors for compressor and turbine models

Parameter	θ_{comp}	θ_{turb}
Nominal shaft speed n_0 [rpm]	70956.37	79998.44
Reference mass flow $\dot{m}_0$ [kg/s]	0.30069	0.46278
Pressure ratio π_0 [-]	1.7999	0.4000
Enthalpy coefficient ψ_0 [-]	0.8000	-4.000
Mach number Ma_0 [-]	0.222	0.500
Sensitivity parameter x [-]	2.000	2.000
Sensitivity parameter y [-]	0.100	0.934
Inlet temperature $T_{in,0}$ [°C]	36.384	500.63

These calibrated parameters were used to generate the compressor and turbine maps shown in Figure 7. Confidence intervals and residual diagnostics were not evaluated in the current study but represent relevant extensions for future work.

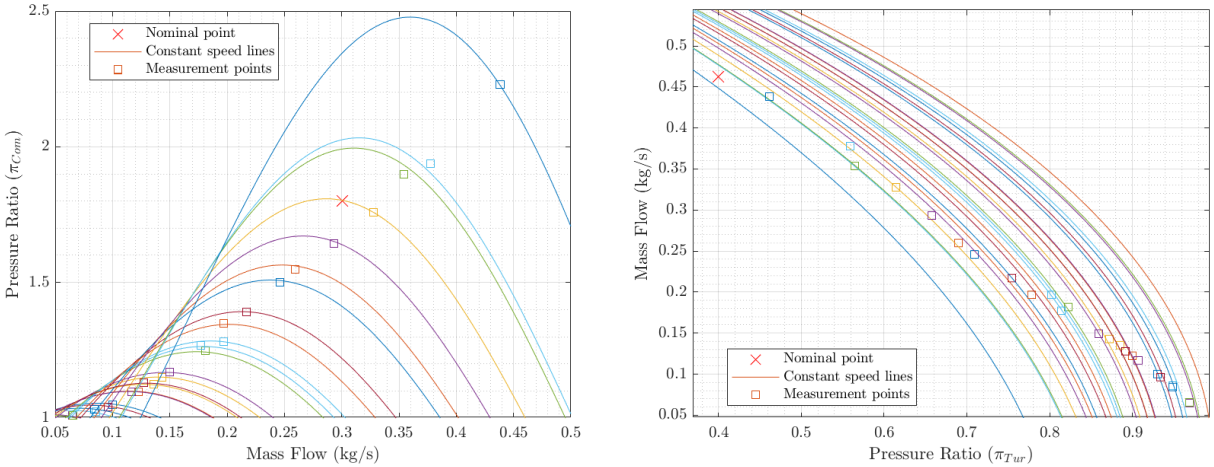

(a) Compressor map

(b) Turbine map

Figure 7: Calibrated compressor and turbine maps. Surge and choke lines are not shown.

2.6 Validation

For model validation, four transient engine measurement runs were performed at different engine speeds, each consisting of three to five consecutive load steps interspersed with steady-state periods, as outlined in Table 3.

To quantify the model's accuracy, the three performance — Mean Absolute Error (MAE), Mean Absolute Percentage Error (MAPE), and the Pearson Product-Moment Correlation Coefficient (PPMCC) — indices described in (Ghelardoni et al., 2013; Coraddu et al., 2022) were calculated for the full run, the steady-state sections, and the dynamic segments.

Table 3: Load profile of validation runs.

Speed [rpm]	**Steady-state power level between steps [kW]**
900	$40 \rightarrow 80 \rightarrow 150 \rightarrow 100$
1050	$40 \rightarrow 80 \rightarrow 150 \rightarrow 100$
1300	$80 \rightarrow 150 \rightarrow 300 \rightarrow 250 \rightarrow 100$
1500	$80 \rightarrow 150 \rightarrow 300 \rightarrow 400 \rightarrow 250 \rightarrow 100$

A full overview of validation errors for all runs is provided in Table 5. Comparison across engine speeds reveals reduced model accuracy at lower speeds, particularly for throttle position and turbo shaft speed. Despite the increase in relative error at low speeds, the correlation coefficients remain consistent across all four load profiles. These coefficients are especially relevant during dynamic phases, as they indicate how closely the simulation tracks the measured data. For most variables, correlation during transients exceeds 85%, suggesting the model reliably captures real engine behaviour. However, a few variables, specifically mass flow and the derived engine efficiency η_{eng}, show significantly lower correlations. This is attributed to a known 3-second delay in the mass flow sensor, as reported by the manufacturer (Instruments), rendering these measurements and the associated efficiency calculations unreliable.

3 Case Study - Results

With the obtained simulation model, five different load-sharing strategies were which are summarized in Table 4 and discussed in the following paragraphs.

Table 4: Scenarios with the summarized control strategy, the amount of energy supplied by the ESS, and the engine stabilizing time after the load step.

Scenario	**Strategy**	**ESS Energy Supply**	**Stabilizing time**
Reference AC	Fixed Speed Load Step	0 kJ	21 s
VSG Without ESS	Simultaneous Speed Step & Load Step	0 kJ	Engine Stall
VSG Long Ramp	Simultaneous Speed Ramp 75 rpm/s & Load Ramp 10 kW/s	1620 kJ	25 s
VSG Long Delay	Speed Ramp 75 rpm/s Load Ramp 100 kW/s after stabilizing	3762 kJ	43 s
VSG Best Option	Speed Ramp 75 rpm/s Load Ramp 100 kW/s after 6 s	1242 kJ	18 s

A reference scenario was simulated for a fixed-speed generator operating at nominal engine speed. After 20 seconds, the load demand was instantaneously increased from 220 kW to 400 kW. The corresponding set points for engine speed and load are shown in Figure 8a. The requested load trajectory is represented by a vertical yellow line in the engine envelope (Figure 8b), while the actual engine response, plotted in red, shows significant deviation from this ideal path. Following the load increase, engine speed initially drops to 1360 rpm before recovering. During acceleration, the engine temporarily delivers substantially more than the requested 400 kW, as additional power is required to regain speed. This results in the engine operating under high load conditions, momentarily exceeding the static engine envelope (indicated by the dashed line). Once the engine speed returns to 1500 rpm, it continues to overshoot, approaching the automatic emergency shutoff threshold of 1650 rpm. Due to the overshoot the engine control system then reduces power, allowing the speed to stabilize again at 1500 rpm, 21 s after the increase in requested power.

This simulation highlights that, for a simple loadstep the actual engine behaviour is more complex due to transient dynamics. Notably, the real load path approaches and briefly exceeds both the engine's load and speed limits, despite the ideal path remaining within safe margins. These transient effects are also reflected in the air-fuel ratio and exhaust gas temperature, as shown in Figures 8c and 8d. Ideally, both parameters should transition smoothly; however, the simulation reveals abrupt fluctuations and a temperature spike reaching 950 K. While short-lived, these transients may contribute to temporarily increased emissions and accelerated engine wear over time due to elevated thermal stresses.

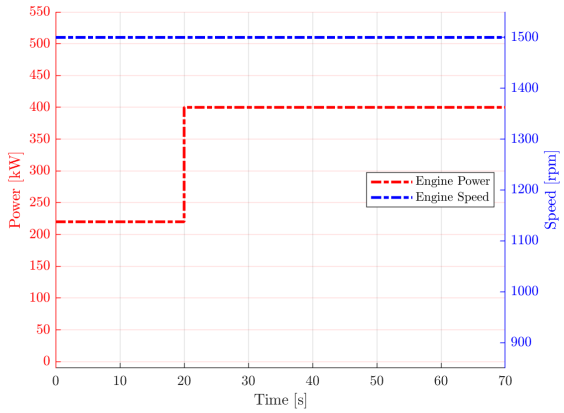

(a) Power and speed (control signal)

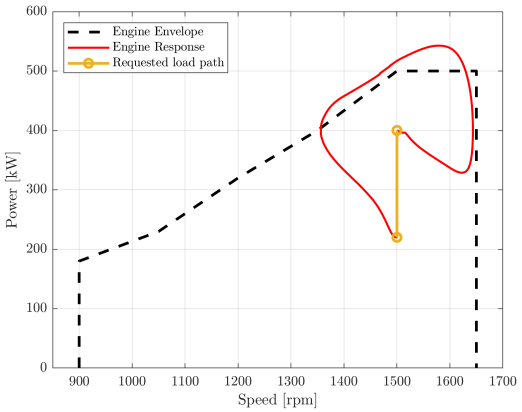

(b) Engine envelope

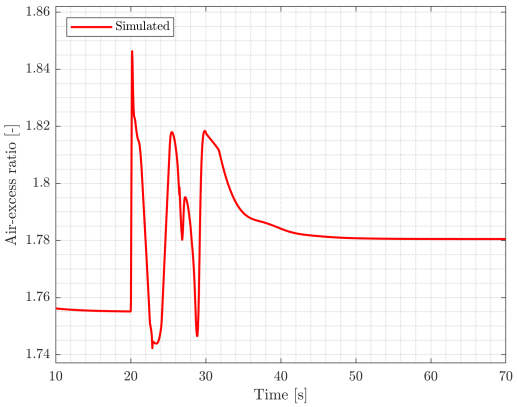

(c) Air-excess ratio

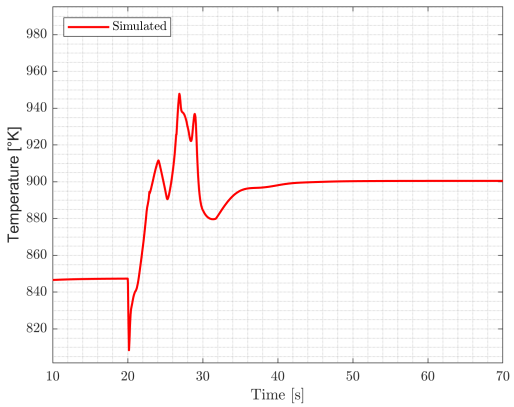

(d) Exhaust temperature

Figure 8: Simulation results for the **Reference AC** scenario

In a variable-speed generator configuration, a change in the requested load alters the engine load point but also necessitates a new engine speed set point. According to the implemented control strategy (see Section 2.3), the same load step from 220 kW to 400 kW requires the engine speed set point to shift instantaneously from 1075 rpm to 1445 rpm, as illustrated in Figure 9a. The requested load trajectory is again represented by a straight yellow line in the engine envelope diagram (Figure 9b). In this scenario, the requested path lies much closer to the engine's static load limit.

This load step demands that the engine delivers significantly more power than it can at the current speed and provides additional power to accelerate to the new speed set point. The throttle valve responds by fully opening—reflected in the spike of the air-excess ratio shown in Figure 9c—yet the resulting engine load substantially exceeds the static limit, as indicated by the red response curve in Figure 9b. In this operating region, the turbocharger cannot supply sufficient air, evidenced by the decreasing air-excess ratio. Consequently, the engine fails to deliver the required power and ultimately stalls. Without support from an energy storage system (ESS), the engine is unable to accommodate such an instantaneous combined step in load and speed.

By integrating an ESS, the initial power demand can be met by the ESS. This allows the engine sufficient time to transit to the new operating point before gradually assuming full power delivery from the ESS. While numerous scenarios can be defined based on the amount of power supplied by the ESS and the rate at which the engine transits, this study considers three scenarios to get more insight.

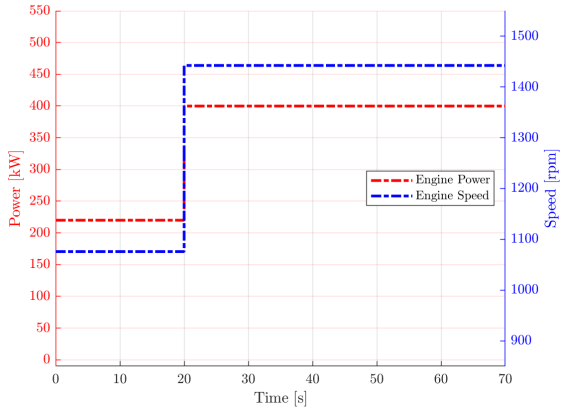

(a) Power and speed (control signal)

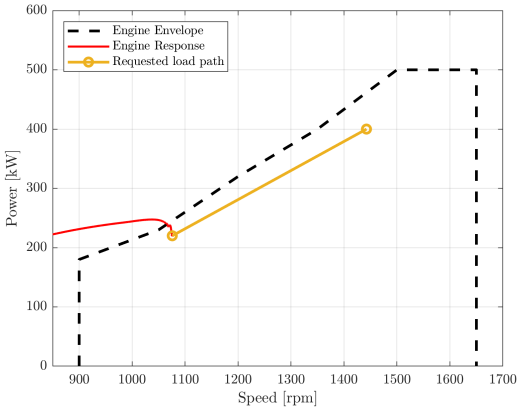

(b) Engine envelope

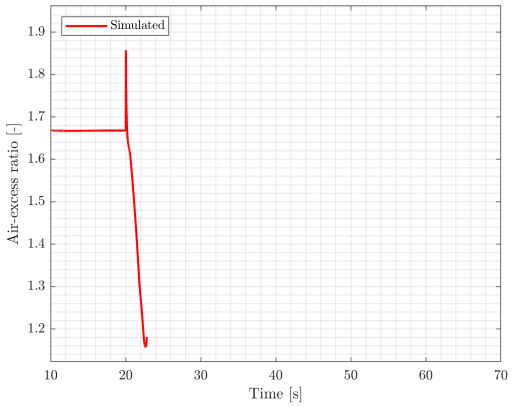

(c) Air-excess ratio

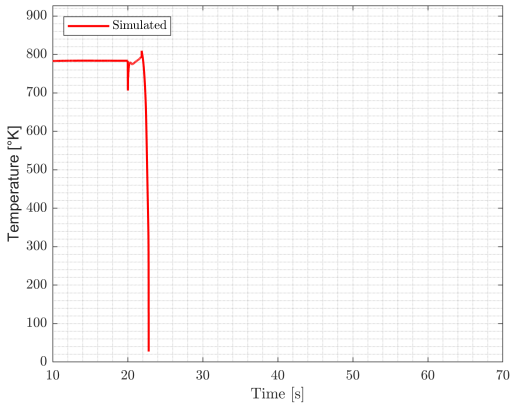

(d) Exhaust temperature

Figure 9: Simulation results for the **VSG Without ESS** scenario

In the first ESS scenario, designated as **VSG Long Ramp**, the engine speed is increased immediately at a steep rate of 75 rpm/s, while the engine load is ramped up simultaneously at a much slower rate of 10 kW/s. During this period, the full grid power demand is initially supplied by the ESS and is gradually transferred to the engine over a duration of 18 seconds, as shown in Figure 10a. The requested load trajectory is again represented in the engine envelope (Figure 10b) by two sequential yellow lines. The engine response, shown in red, indicates a high but non-critical load level, followed by a pronounced overshoot in engine speed.

As a result of the prolonged high load period, the exhaust gas temperature reaches a peak of 985 K, exceeding the maximum temperature observed in the **Reference AC** scenario. Although the simulated engine speed stabilizes at the target value of 1445 rpm approximately 25 s after the load increase, the transient overshoot to 1680 rpm would trigger an automatic emergency shutdown in a real system.

In the scenario labeled **VSG Long Delay**, the engine speed is immediately increased at a rate of 75 rpm/s, after which the engine is allowed to stabilize at the new speed set point. Twenty seconds later, the power demand from the grid is transferred from the ESS to the engine at a rate of 100 kW/s (see Figure 11a). In the engine envelope diagram (Figure 11b), the requested load trajectory, shown in yellow, resembles that of the previous scenario. However, the actual engine response, plotted in red, clearly reveals two distinct phases: a speed increase phase followed by a load application phase.

During the speed ramp-up, the engine load remains well within the static load limits. The subsequent load increase, occurring while the engine is already operating at its target speed, closely mirrors the behaviour observed in the **Reference AC** scenario. Consequently, the thermal response is more moderate, with exhaust temperatures lower than in the **VSG Long Ramp** scenario and comparable to those of the reference scenario, see Figure 11d The engine reaches steady-state operation after approximately 43 seconds. However, the prolonged period of fluctuating air-excess ratio during the transition may lead to extended intervals of elevated emissions. It is worth noting that the delay between the speed and load transitions could be shortened to reduce the overall settling time.

The final scenario labeled **VSG Best Option** aims to exploit the engine's natural overshoot and momentary

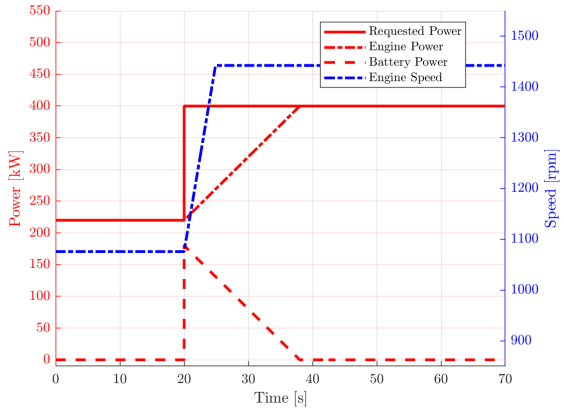

(a) Power and speed (control signal)

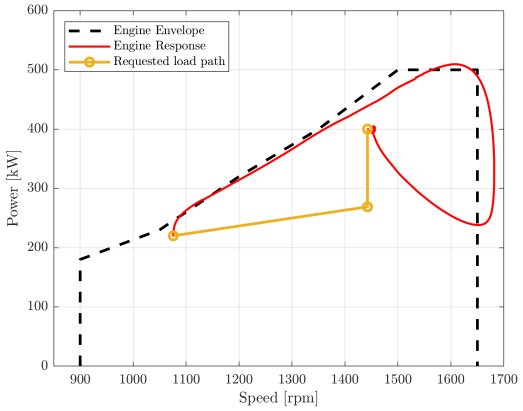

(b) Engine envelope

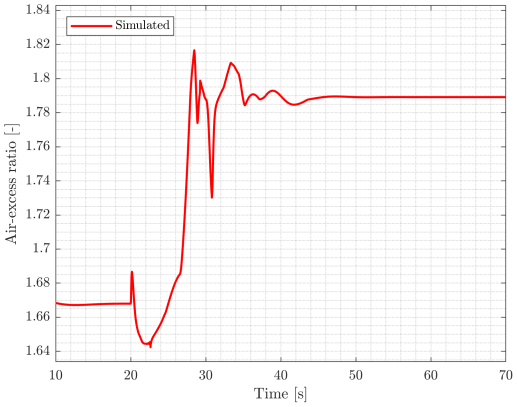

(c) Air-excess ratio

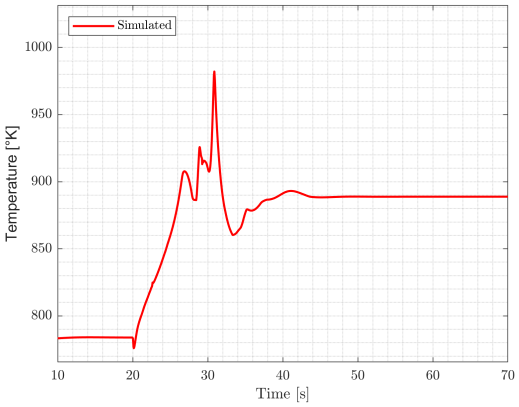

(d) Exhaust temperature

Figure 10: Simulation results for the **VSG Long Ramp** scenario

excess power output to improve system performance. This is achieved by synchronizing the load ramp with the onset of engine speed overshoot—i.e., shortly after the engine exceeds its speed set point, see Figure 12a. By aligning the load increase with this transient, the strategy reduces the magnitude of the overshoot while simultaneously utilizing the surplus energy in a beneficial manner. This approach introduces a delay of 6 seconds between the start of the speed ramp and the onset of the load ramp, with the ramp rates for speed and load kept identical to the previous scenarios.

The resulting engine response is shown in Figure 12b. During both, the speed and load transitions, the engine remains within its static load limit, indicating that this method effectively avoids overloading. Furthermore, engine speed overshoot is reduced to a minimum. As such, this strategy appears to offer the most favourable dynamic behaviour among the tested scenarios. In this scenario, engine reaches steady-state operation after approximately 18 seconds, 3 seconds faster than the reference scenario. Importantly, this approach also minimizes fluctuations and overshoot in both exhaust gas temperature and air–excess ratio (Figures 12c and 12d), contributing to improved emission characteristics and reduced thermal stress.

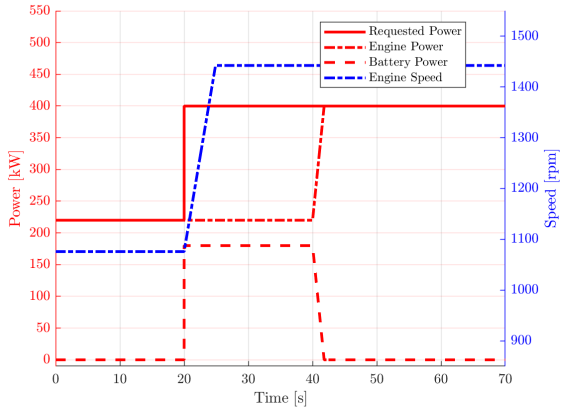

(a) Power and speed (control signal)

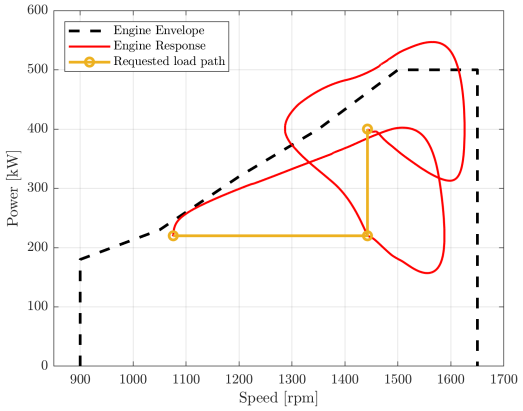

(b) Engine envelope

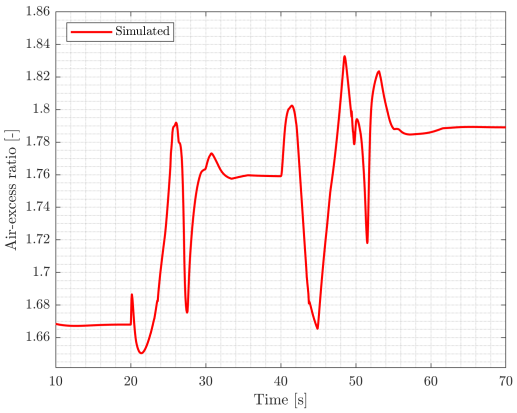

(c) Air-excess ratio

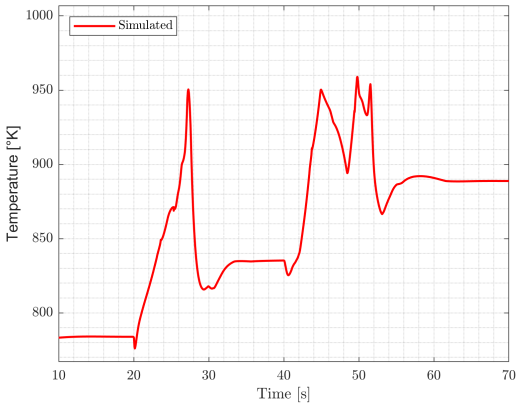

(d) Exhaust temperature

Figure 11: Simulation results for the **VSG Long Delay** scenario

4 Conclusions and Future Work

This research investigated different load sharing strategies to cope with the challenges that occur during load steps on variable speed generators. This investigation is done on a MVEM of a Caterpillar high-speed, spark-ignited gas engine. Unique to this model is the consideration of scavenging losses in the in-cylinder process. The model is calibrated based on static engine data at different load and speed settings. The data set is similar to data that will be provided during the FAT of the new ASWF generators. As a result, the calibration method used in this research can be used for these engines as well.

The validation showed that the correlation of the model is high, around 0.99 for steady state and 0.90 for dynamic segments. For speeds between 1050 rpm and 1500 rpm, the relative error does not go above 10% except for the turbo shaft speed. During dynamic segments, the model is less accurate with a relative error that is up to 10%pt higher for some variables. The validation profile at 900 rpm showed an even higher error, for both steady state and dynamic segments, indicating a less accurate representation of real-world behaviour at low speeds.

The inaccuracy of the model for low speeds can partially be attributed to a poor calibration of the in-cylinder process at these working points. Further investigation should look into these effects. The problem appears to be related to the polynomial fitting of the Seiliger parameters, not taking these data points into account for the fitting appears to make the model more accurate around these points of low speed while decreasing accuracy for higher speeds. This effect seems counter-intuitive; further research could clarify this phenomena.

The strategies that were investigated were the use of a long ramp, a long delay and a best timed option. During the testing of these strategies, it was discovered that the engine reacts way better on ramps instead of steps. This is true for both changes in speed and load set point. In addition to that, a delay between the speed change and load change greatly improved the load response. This method enables the engine to first increase engine speed before having to deal with a load step. The best result has been obtained when the load ramp starts around at the moment the engine crosses its new speed set point the first time. In this way, the overshoot in engine speed

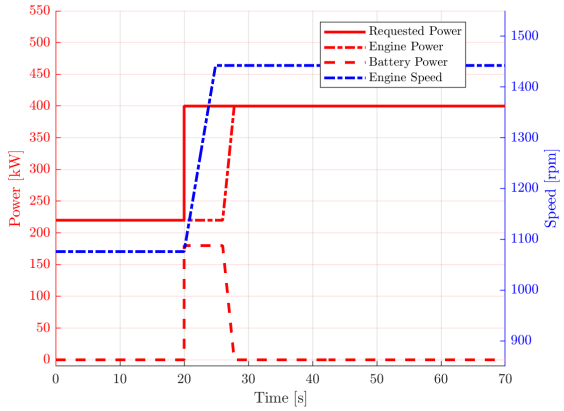

(a) Power and speed (control signal)

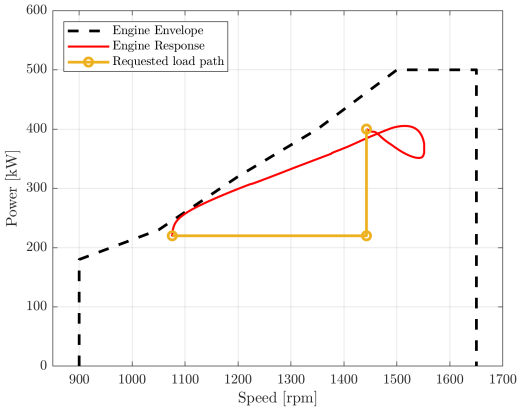

(b) Engine envelope

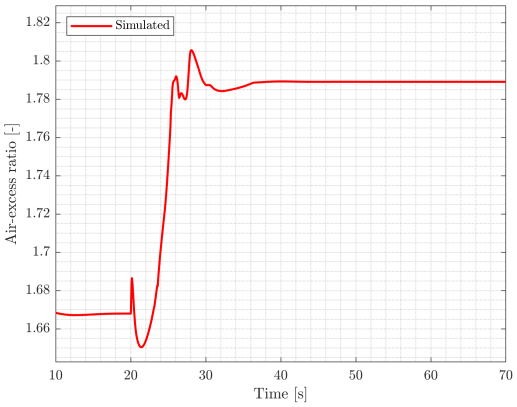

(c) Air-excess ratio

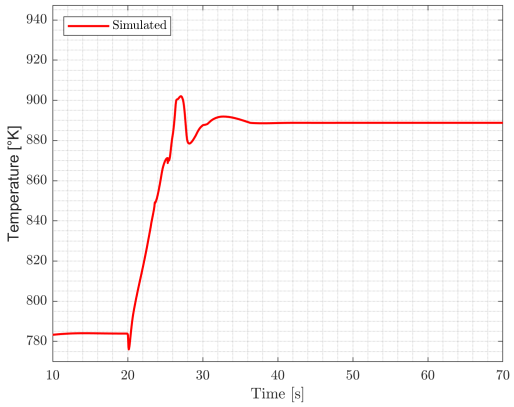

(d) Exhaust temperature

Figure 12: Performance metrics for the **best option** scenario.

is used beneficially, and the engine reaches its new set point the fastest way possible without going outside the engine envelope. In conclusion, ESS and load-sharing strategies can improve the load response of variable speed generators.

On the other hand, one of the main limitations of this research is the limitation of the battery. This research approached the battery as an Energy Storage System without any limitations. In reality, there are limitations on the maximum current output and capacity of batteries that were not taken into account. Further research could model these limitations and investigate the feasibility of the proposed strategies with batteries and look for alternative ESS if batteries are not suitable. Furthermore, this research only investigates load steps that could be fully covered by the battery. An interesting follow-up study would be the evaluation of partial power take-over and the effect on the optimal load-sharing strategy.

Acknowledgement

The authors would like to thank the staff of the engine laboratory of the Netherlands Defence Academy (NLDA) for their support and assistance during the measurement campaign.

The authors acknowledge the use of OpenAI's ChatGPT to support the refinement of writing style and language clarity. No AI-generated content was used for the development of ideas, analysis, or conclusions presented in this paper.

References

Ayers, W.N., 2022. Dc grids for ship propulsion: Benefits and challenges, in: SNAME Maritime Convention, SNAME. p. D031S017R004.

Bellache, K., Camara, M.B., Dakyo, B., 2017. Transient power control for diesel-generator assistance in electric boat applications using supercapacitors and batteries. IEEE Journal of Emerging and Selected Topics in Power Electronics 6, 416–428.

Bø, T.I., Vaktskjold, E., Pedersen, E., Mo, O., 2019. Model predictive control of marine power plants with gas engines and battery. IEEE Access 7, 15706–15721.

Bosklopper, J., Sapra, H., van de Ketterij, R., van Sluijs, W., Bekdemir, C., de Vos, P., Visser, K., 2020. Experimental study on a retrofitted marine size spark-ignition engine running on port-injected 100% methanol. INEC 2020, Delft .

Boujelben, M., Trigui, R., 2021. Optimal power control for a variable-speed generator integrated in series hybrid vehicle. IEEE Transactions on Transportation Electrification 8, 1302–1312.

Brekelmans, G.T.R., 2024. Defensienota 2024 sterk, slim en samen. Technical Report. MINISTERIE VAN DEFENSIE.

Coraddu, A., Oneto, L., Cipollini, F., Kalikatzarakis, M., Meijn, G.J., Geertsma, R., 2022. Physical, data-driven and hybrid approaches to model engine exhaust gas temperatures in operational conditions. Ships and Offshore Structures 17, 1360–1381.

Drakoulas, M., Reurings, J., Meijn, G., Wittingen, M., 2022. Adaptive pitch control: Simulation performance evaluation against conventional propulsion control, in: Conference Proceedings of INEC, pp. 1–13.

Eberhart, R., Shi, Y., 2001. Comparing genetic algorithms and particle swarm optimization. Proceedings of the 2001 Congress on Evolutionary Computation (CEC) , 611–616URL: https://doi.org/10.1109/CEC.2001.934374, doi:10.1109/CEC.2001.934374.

Farrier, L., Bucknall, R., 2020. Investigating the performance capability of a lithium-ion battery system when powering future pulsed loads. Energies 13, 1357.

Gattozzi, A., Herbst, J., Hebner, R., Blau, J., Cohn, K., Colson, W., Sylvester, J., Woehrman, M., 2015. Power system and energy storage models for laser integration on naval platforms, in: 2015 IEEE Electric Ship Technologies Symposium (ESTS), IEEE. pp. 173–180.

Geertsma, R., Negenborn, R., Visser, K., Hopman, J., 2017a. Parallel control for hybrid propulsion of multifunction ships. IFAC-PapersOnLine 50, 2296–2303.

Geertsma, R., Negenborn, R., Visser, K., Loonstijn, M., Hopman, J., 2017b. Pitch control for ships with diesel mechanical and hybrid propulsion: Modelling, validation and performance quantification. Applied energy 206, 1609–1631.

Ghelardoni, L., Ghio, A., Anguita, D., 2013. Energy load forecasting using empirical mode decomposition and support vector regression. IEEE Transactions on Smart Grid 4, 549–556. doi:10.1109/TSG.2012.2235089.

Haseltalab, A., Botto, M.A., Negenborn, R.R., 2019. Model predictive dc voltage control for all-electric ships. Control Engineering Practice 90, 133–147.

Horlock, J.H., Winterbone, D., 1986. The thermodynamics and gas dynamics of internal-combustion engines. Volume II. New York, NY; Oxford University Press.

Instruments, S., . QuadraTherm 640i-780i. QTherm V3.

Iwanski, G., Bigorajski, Ł., Koczara, W., 2018. Speed control with incremental algorithm of minimum fuel consumption tracking for variable speed diesel generator. Energy conversion and management 161, 182–192.

Kalikatzarakis, M., Coraddu, A., Theotokatos, G., Oneto, L., 2021. Development of a zero-dimensional model and application on a medium-speed marine four-stoke diesel engine, in: 3rd International Conference on Modelling and Optimisation of Ship Energy Systems.

Kennedy, J., Eberhart, R., 1995. Particle swarm optimization, in: Proceedings of ICNN'95 - International Conference on Neural Networks, IEEE. pp. 1942–1948. URL: https://doi.org/10.1109/ICNN.1995.488968, doi:10.1109/ICNN.1995.488968.

Kim, S., Jeon, H., 2022. Comparative analysis on ac and dc distribution systems for electric propulsion ship. Journal of Marine Science and Engineering 10, 559.

Kiouranakis, K.I., Vos, P.d., Willems, R., Sapra, H.D., Geertsma, R., 2025. Dual-phase combustion behavior in a converted marine natural gas si engine: Exploring the impact of bowl-in and squish phases on performance and emissions. Applied Thermal Engineering 269, 1–26.

Mobarra, M., Rezkallah, M., Ilinca, A., 2022. Variable speed diesel generators: Performance and characteristic comparison. Energies 15, 592.

Nocedal, J., Wright, S.J., 2006. Numerical Optimization. Springer Science & Business Media. URL: https://doi.org/10.1007/978-0-387-40065-5, doi:10.1007/978-0-387-40065-5.

Roos, W., 2025. Performance Analysis of Variable Speed Diesel Generators in Naval Hybrid DC Power Supply rchitectures. Master's thesis. TU Delft.

Roos, W., Vollbrandt, J., Coraddu, A., Geertsma, R., 2025. Variable speed generators for dc hybrid power supply of naval vessels. Concept of journal paper MOSES 2025.

Saponaro, G., Stefanizzi, M., D'Amato, D., Franchini, E., Fornarelli, F., Torresi, M., Camporeale, S.M., 2022. Modeling and design optimization of a hybrid power generator for full-electric naval propulsion, in: Journal of Physics: Conference Series, IOP Publishing. p. 012087.

Sapra, H., Linden, Y., van Sluijs, W., Godjevac, M., Visser, K., 2019. Experimental investigations of performance variations in marine hydrogen-natural gas engines, in: Cimac Congress, pp. 1–17.

Schulten, P., Geertsma, R., Visser, K., 2017. Energy as a weapon, part ii, in: EAAW VII: International Symposium Engine As A Weapon, IMarEST. pp. 1–10.

Seiliger, M., 1926. Die Hochleistungs-Dieselmotoren. J. Springer.

Smith, N., 2019. Energy as a weapon-architecture reloaded, in: Conference Proceedings of EAAW, pp. 1–9.

Stapersma, D., 2019. A general model for off-design performance of a single stage turbomachine. Technical Report. Delft University of Technology. Issue e.

Stutevant, G., Voth, J., Sorrentino, V., Pence, E., 2022. A moment of maritime opportunity? the operational energy challenge, in: Conference Proceedings of INEC, pp. 1–14.

Van't Hart, S., WALRAVEN, G., Takken, E., 2024. Het anti-submarine warfare fregat. Technical Report. Marineblad KVMO.

Vollbrandt, J., Coraddu, A., Geertsma, R., 2024. Hybrid turbocharging for alternatively fueled internal combustion engines in naval applications, in: Conference Proceedings of iSCSS, pp. 1–13.

Vollbrandt, J., Coraddu, A., Geertsma, R.D., Stapersma, D., 2025. High-fidelity mean value first principle modeling of dynamic response in spark-ignited marine engines: A comparative analysis of gas path and turbocharger representations. Concept of journal paper JMET.

Voskuijl, M., Dekkers, T., Savelsberg, R., 2020. Flight performance analysis of the samad attack drones operated by houthi armed forces. Science & Global Security 28, 113–134.

Voth, J.M., Pence, E.G., Sorrentino, V., Sturtevant, G.H., 2024. A moment of maritime opportunity? the us navy operational energy challenge. Journal of Marine Engineering & Technology 23, 196–208.

Whitelegg, I., Pawling, R.J., Bucknall, R.W., 2014. The impact of pulse loads on electric warship power systems, in: SNAME Maritime Convention, SNAME. p. D011S001R009.

Zahedi, B., Norum, L.E., Ludvigsen, K.B., 2014. Optimized efficiency of all-electric ships by dc hybrid power systems. Journal of power sources 255, 341–354.

Zak, A., 2008. Ships classification basing on acoustic signatures. WSEAS Transactions on Signal Processing 4, 137–149.

5 Tables

Table 5: Performance metrics of validation run at different engine speeds.

Variable	mae	mape	ppmcc	mae_ss	mape_ss	ppmcc_ss	mae_dyn	mape_dyn	ppmcc_dyn
900 RPM									
P_b [kW]	2.88	2.79	0.98	1.12	1.45	1.00	9.66	7.96	0.91
n_{eng} [rpm]	5.36	0.61	0.86	1.30	0.14	0.05	20.91	2.37	0.88
thr_{pos} [%]	9.29	19.62	0.92	7.11	16.92	0.95	17.59	29.93	0.89
n_{tc} [rpm]	6969.72	47.33	0.99	7620.74	53.38	0.99	4562.14	25.97	0.97
P_{ac} [kPa]	7.67	7.27	0.90	8.11	7.71	0.91	6.02	5.61	0.87
P_{ir} [kPa]	12.71	15.31	0.98	12.46	15.60	0.99	13.75	14.40	0.94
P_{er} [kPa]	15.63	14.58	0.90	17.86	16.69	0.92	7.70	7.10	0.81
η_{eng} [%]	1.27	4.72	0.95	1.01	3.88	0.99	2.29	8.00	0.70
dm_{in} [kg/s]	0.03	13.13	0.95	0.03	12.67	0.99	0.04	14.92	0.81
m_f [kg/s]	0.00052	5.38	0.98	0.00046	5.05	1.00	0.00077	6.79	0.91
1050 RPM									
P_b [kW]	2.16	2.23	0.99	1.25	1.45	1.00	8.71	7.97	0.94
n_{eng} [rpm]	2.61	0.25	0.90	1.30	0.12	-0.10	12.02	1.16	0.94
thr_{pos} [%]	2.44	6.31	0.96	2.21	5.86	0.96	4.09	9.60	0.98
n_{tc} [rpm]	4588.78	27.11	0.96	4704.63	28.06	0.97	3925.42	22.34	0.93
P_{ac} [kPa]	5.25	4.90	0.94	5.34	4.99	0.95	4.70	4.37	0.90
P_{ir} [kPa]	5.05	6.64	0.98	4.92	6.62	0.99	6.12	7.18	0.96
P_{er} [kPa]	9.86	9.13	0.81	10.29	9.54	0.81	7.88	7.22	0.80
η_{eng} [%]	1.09	4.39	0.95	0.86	3.50	0.99	2.72	10.93	0.74
dm_{in} [kg/s]	0.01	6.54	0.95	0.01	5.38	0.99	0.03	15.03	0.74
m_f [kg/s]	0.00049	4.69	0.99	0.00047	4.63	0.99	0.00062	5.39	0.97
1300 RPM									
P_b [kW]	7.69	3.37	0.97	2.41	1.35	1.00	29.15	11.60	0.84
n_{eng} [rpm]	5.47	0.42	0.86	0.85	0.07	-0.31	24.26	1.89	0.86
thr_{pos} [%]	3.52	7.00	0.95	2.78	5.91	0.98	6.52	11.38	0.95
n_{tc} [rpm]	1679.46	4.78	0.99	1347.82	4.20	0.99	3035.39	7.19	0.93
P_{ac} [kPa]	3.63	2.80	0.97	2.87	2.33	1.00	6.73	4.74	0.89
P_{ir} [kPa]	5.42	5.00	0.98	4.41	4.34	0.99	9.57	7.68	0.92
P_{er} [kPa]	2.77	2.13	0.98	2.46	1.96	1.00	3.99	2.80	0.94
η_{eng} [%]	1.18	4.00	0.92	0.77	2.65	1.00	2.83	9.40	0.51
dm_{in} [kg/s]	0.04	8.23	0.94	0.03	6.17	1.00	0.08	16.68	0.72
m_f [kg/s]	0.00064	3.39	0.98	0.00044	2.49	1.00	0.00149	7.09	0.92
1500 RPM									
P_b [kW]	5.54	2.60	0.99	2.35	1.22	1.00	20.46	9.03	0.95
n_{eng} [rpm]	2.63	0.18	0.82	1.01	0.07	-0.02	10.25	0.69	0.87
thr_{pos} [%]	3.92	8.47	0.94	2.87	7.11	0.95	7.56	17.04	0.90
n_{tc} [rpm]	1642.47	3.57	0.98	1098.90	2.31	1.00	4183.95	9.47	0.91
P_{ac} [kPa]	4.67	3.21	0.97	3.52	2.37	1.00	10.08	7.12	0.86
P_{ir} [kPa]	2.95	2.86	0.98	2.31	2.27	1.00	6.00	5.70	0.96
P_{er} [kPa]	4.61	2.98	0.98	4.14	2.70	1.00	6.79	4.30	0.97
η_{eng} [%]	0.68	2.42	0.95	0.39	1.33	0.98	2.01	7.56	0.76
dm_{in} [kg/s]	0.03	5.83	0.98	0.02	4.30	1.00	0.06	12.96	0.89
m_f [kg/s]	0.00044	2.39	0.98	0.00033	1.82	1.00	0.00097	5.10	0.96

Table 6: Air-to-fuel ratio (λ) lookup table as a function of engine load (%) and speed (rpm).

Speed (rpm)	**10%**	**20%**	**30%**	**40%**	**50%**	**60%**	**70%**	**80%**	**90%**	**100%**	**110%**
0	0.996	0.996	0.996	0.996	0.996	0.996	0.996	0.996	0.996	0.996	0.996
250	1.000	1.000	1.000	1.000	1.000	1.000	1.000	1.000	1.000	1.000	1.000
500	1.046	1.046	1.046	1.046	1.046	1.026	1.026	1.026	1.026	1.026	1.026
700	1.146	1.146	1.146	1.146	1.146	1.126	1.126	1.126	1.126	1.125	1.125
800	1.120	1.245	1.380	1.390	1.400	1.400	1.400	1.400	1.400	1.400	1.400
898	1.120	1.245	1.380	1.390	1.400	1.400	1.400	1.400	1.400	1.400	1.400
1020	1.120	1.245	1.360	1.390	1.400	1.400	1.400	1.400	1.400	1.400	1.400
1170	1.190	1.267	1.320	1.385	1.415	1.420	1.430	1.430	1.430	1.430	1.430
1319	1.190	1.267	1.352	1.389	1.410	1.446	1.474	1.496	1.506	1.506	1.506
1340	1.190	1.282	1.393	1.390	1.400	1.441	1.476	1.461	1.481	1.471	1.471
1459	1.190	1.272	1.330	1.356	1.394	1.397	1.421	1.436	1.416	1.436	1.446
1471	1.240	1.282	1.320	1.326	1.369	1.402	1.432	1.434	1.435	1.454	1.475
1500	1.240	1.282	1.320	1.326	1.369	1.402	1.432	1.434	1.435	1.454	1.475
1600	1.240	1.282	1.320	1.326	1.369	1.402	1.432	1.434	1.435	1.454	1.475
1700	1.270	1.312	1.350	1.356	1.399	1.420	1.462	1.464	1.465	1.484	1.505